Journal of the European Ceramic Society 44 (2024) 328–340

Contents lists available at ScienceDirect

Journal of the European Ceramic Society

journal homepage: www.elsevier.com/locate/jeurceramsoc

Ultra-rapid debinding and sintering of additively manufactured ceramics by ultrafast high-temperature sintering

Subhadip Bhandari [a], Charles Manière [b], Francesco Sedona [c], Emanuele De Bona [d], Vincenzo M. Sglavo [d,e], Paolo Colombo [a,f], Luca Fambri [d,e], Mattia Biesuz [d,e,*], Giorgia Franchin [a,**]

[a] Department of Industrial Engineering, University of Padova, Via Marzolo 9, Padova 35131, Italy
[b] ENSICAEN, UNICAEN, CNRS,CRISMAT, Normandie Univ, Caen, France
[c] Department of Chemical Sciences, University of Padova, Via Marzolo 1, Padova 35131, Italy
[d] Department of Industrial Engineering, University of Trento, Via Sommarive 9, Trento 38123, Italy
[e] INSTM, Via G. Giusti 9, Firenze 50121, Italy
[f] Department of Materials Science and Engineering, The Pennsylvania State University, University Park, PA, USA

ARTICLE INFO

Keywords:
Ultrafast high-temperature sintering
YSZ
Additive manufacturing
Fused filament fabrication
Debinding

ABSTRACT

In recent years, additive manufacturing (AM) of ceramics has significantly advanced in terms of the range of equipment available, printing resolution and productivity. Most techniques involve the use of ceramic powders embedded in an organic binder which is typically removed through a slow thermal debinding process.

Herein, we prove for the first time that ultra-rapid debinding and sintering are possible for complex 3YSZ components produced using material extrusion technology. The printed components were first chemically debinded in acetone thus removing about one-half of the binder, and then thermally debinded and densified by ultrafast high-temperature sintering (UHS) in a single-step process (30–120 s). Fully dense components were obtained with tailored microstructure and nanometric grain size. The sintered artefacts were crack-free even at the microscopic level.

This approach paves the way for rapid processing (debinding and sintering) of additively manufactured ceramics with reduced energy consumption and carbon footprint.

1. Introduction

Powder shaping and sintering is one of the most successful processes developed by mankind over the centuries [1]. The first sintered artefacts date back to 25,000 BCE; however, high-temperature firing is still the fundamental process in ceramic technology and, nowadays, it is applied to wider classes of materials including metals, cermets, metallic glasses, and preceramic polymers.

Concerning powder shaping technologies, traditional processes (slip casting [2], tape-casting [3], extrusion, pressing, and injection molding [4]) are currently challenged by new shaping procedures. Among them, revolutions in numerical control and process automation have allowed the development of additive manufacturing (AM) technologies. These techniques have the potential to overcome some limitations related to traditional shaping, especially when considering complex geometries [5]. In fact, AM enables the production of complex structures with high accuracy and reduced labor costs. As a result, AM has attracted widespread scientific and technical interest since its inception in the 1980s [6].

In the past few years, there has been considerable development and growth of AM technologies related to metallic and polymeric components. On the contrary, the implementation of AM technologies in the field of ceramics has been sluggish [7]. This technological delay is related to the complexity of ceramics processing and not to a lack of technological interest. It could be argued that the shaping of ceramics would benefit more from AM than any other material family. Indeed, ceramics can be hardly machined by subtractive technologies, making it not straightforward to fabricate the complex shapes that could easily be realised in metallic components.

Although additive manufacturing of ceramics is still not yet common

* Corresponding author at: Department of Industrial Engineering, University of Trento, Via Sommarive 9, Trento 38123, Italy.
** Corresponding author.
E-mail addresses: mattia.biesuz@unitn.it (M. Biesuz), giorgia.franchin@unipd.it (G. Franchin).

https://doi.org/10.1016/j.jeurceramsoc.2023.08.040
Received 18 July 2023; Received in revised form 21 August 2023; Accepted 23 August 2023
Available online 25 August 2023
0955-2219/© 2023 The Author(s). Published by Elsevier Ltd. This is an open access article under the CC BY license (http://creativecommons.org/licenses/by/4.0/).

at the industrial level, a variety of technologies are being developed and adapted, including stereolithography (SLA), binder jetting (BJ), direct ink writing (DIW), etc. [7]. All of the aforementioned technologies usually require either expensive equipment (compared to that employed for polymers) or expert tuning of the feedstock. On the other hand, fused filament fabrication (FFF) of ceramics-loaded filaments employs relatively inexpensive equipment meant for polymeric materials, with little adaptation of the process parameters, potentially enabling a broader diffusion of AM ceramic components [8,9].

Green components can be produced very quickly by FFF technology, but they still require long and accurate debinding and sintering treatments to obtain the final ceramic components [8,10,11]. Thus, there is a real need to develop routes involving both innovative shaping and sintering routes to decrease the overall processing time.

In the past couple of years, the ultrafast high-temperature sintering (UHS) technique has been developed and used [12] to densify several ceramics in a few seconds [13–25]. In a typical UHS setup, the green body is sandwiched between carbon felts that are connected to an electrical power source [26]. As the power supply is turned on, the heat produced by the Joule effect in the felts is transferred to the green body, allowing ultrafast heating and cooling ($\approx 10^4$-10^5 °C min^{-1}) and causing densification in a few seconds-minutes [27].

Proofs-of-concept for rapid sintering of printed components have already been reported [12,28,29]; nevertheless, the bottleneck of the process is still represented by the thermal debinding step, which is typically carried out at heating rates of approximately 0.1–0.3 °C min^{-1}, thus impacting on the productivity, the energy demand, and carbon footprint [10,30]. To date, the fundamental question "*Is it possible to achieve rapid thermal debinding and sintering of fused filament fabricated (FFF) ceramics in a single step?*" lacks an answer.

On these bases, herein, we studied the UHS of 3 mol% yttria-stabilized zirconia (YSZ) components printed via FFF as a model ceramic system. Moreover, the optimization of preliminary chemical debinding and the optimal UHS conditions allow a single-step thermal debinding/sintering process to occur in the order of tens of seconds were identified.

2. Experimental procedure and method

2.1. Starting material and sample preparation

A commercial YSZ white zirconia filament from Zetamix (Nanoe, France) was used as feedstock to print the green bodies; the filament had a diameter of 1.75 mm and contained 50 vol% YSZ powder (d_{01} = 0.1 μm, d_{50} = 0.3 μm, d_{99} = 2 μm) embedded in an organic binder system [31]. The true density of the powder (extracted from the filament by thermally degrading the binder at 600 °C), as measured by a helium gas pycnometer (Ultrapyc 3000, Anton Paar) was found to be 5.995 ± 0.008 g cm^{-3}.

In order to validate the rapid debinding and sintering of the AMed ceramic components, a complex and intricate geometry was required which cannot be traditionally shaped by conventional fabrication techniques. The gyroidal pattern, i.e., a triply periodic minimal surface (TPMS) cellular structure, is often chosen as a proof of concept for AMed components with high complexity. Such geometry possesses a high strength-to-weight ratio, making it useful in applications including structural weight reduction, biomedical, and aerospace, and a high porosity and surface accessibility essential for applications such as heat exchangers, and catalyst carriers. While no specific application is sought in this work, we thought that this specific infill pattern would provide for a meaningful proof-of-concept. Disk-shaped components (diameter = 10.1 mm; thickness = 3.1 mm) were designed with a gyroidal infill pattern with 25 % density; they were then fabricated using a fused filament printer (Raise 3D Pro) with a 0.4 mm diameter nozzle. An optical picture of the printed green body along with the optimized printing/slicing parameters used for this particular study is shown in Fig. S1.

Three different materials were subjected to UHS: (i) as-printed; (ii) partially chemically debinded and (iii) partially chemically debinded and pre-sintered (950 °C for 1 h). The printed samples were soaked in acetone (Sigma Aldrich, purity 99.5 %) at 40 °C for increasing times (up to 4 h, as per the technical datasheet) to carry out the chemical debinding. After 1 h, the chemical debinding process allows the removal of a little more than 50 % of the organic binder (i.e., the soluble binder fraction), with modest variations being recorded for longer soaking times. Since as-printed samples during UHS did not retain the shape and the pre-sintered ones showed extensive cracking, we focused most of the analysis on partially chemically debinded green bodies (1 h of debinding in acetone).

2.2. Ultra-fast high-temperature sintering (UHS)

UHS was carried out using a graphite felt (SGL carbon Co., Germany) clamped between two steel plates and connected to a DC power source (Agilent 6674 A). The sample was introduced in the center of the felt by producing a small horizontal cut on the felt. The felt cross section was 24 × 6 mm^2 (nominal thickness = 5 mm, the thickness measured with a caliper was about 6 mm) and the span between the steel electrodes was 30 mm. The small aperture made in the graphite felt was closed with a piece of the felt to minimize heat losses and homogenize the temperature distribution. The felt containing the sample was introduced into a borosilicate glass flask (Fig. S2) which was evacuated and subsequently filled with Ar; a vigorous Ar flux was maintained throughout the experiment. UHS was carried out by applying (in a single step) different currents for different holding times to induce Joule heating in the felt, as reported in Table S1. The electric data was acquired with a digital multimeter (Keithley 2100) at 1 Hz.

For comparison, conventional sintering experiments were carried out in air and Ar atmosphere at 1475 °C with a dwell time of 2 h. The comparison of a typical sintering profile for 3D printed parts produced from zirconia filaments and that recorded upon UHS is shown in Fig. S3.

2.3. Finite element modelling (FEM) of the UHS heating

UHS involves different physics, comprising the Joule heating of the graphite felt, radiative/convective heat fluxes, debinding/sintering of the printed specimen, and grain growth.

In this study, the heating of the felt and 3D-printed specimen was simulated. The estimated felt temperature was calibrated with the melting point of high-purity metals (Cu, Ni, and Pt). To avoid a time-consuming fluid dynamic simulation [32,33], convective heat losses were modeled by convective fluxes also calibrated experimentally. The surface-to-surface radiation was applied in the inner felt zones to simulate the heat exchanges between the felt and the sample, and also inside the complex gyroid structure. The thermal properties assigned to porous zirconia, together with the physics and boundary conditions equations, are detailed elsewhere [34]. The calibrated electro-thermal properties of the graphite felt and the steel electrode properties are reported in Table 1.

The electro-thermal simulations of the UHS tests were carried out using Comsol® and include the steel electrode, the graphite felt and the 3D-printed zirconia gyroïd sample. Because this sample is centimetric in size, it is difficult to evaluate the contact and closure quality. Consequently, two simulations were performed. One is called "full contact" which assumes that the external surfaces of the specimen are in full contact with the felt and there is no aperture for convection losses. The other assumes that the sample external surfaces are not in contact with the felt and convection fluxes similar to those observed with the calibration tests are present due to the aperture in the felt (chimney effect). Inner convection losses were mandatory for the calibration tests (similar conditions of the contactless configuration); it gives the following convection coefficient formula for the sample and inner felt surfaces:

Table 1
Steel and graphite felt electro-thermal properties; the steel properties and graphite felt specific heat were taken from [35]; the felt thermal properties were taken from [36], only the felt electrical conductivity was calibrated.

Material properties	Materials	
	Graphite felt	Steel electrode
Thermal conductivity (W m^{-1} K^{-1}))	$0.019e^{0.0015T}$	$9.99 + 0.0175T$
Specific heat (J kg^{-1} K^{-1}))	$34.3 + 2.72T - 9.610^{-4}\ \ T^2$	$446.5 + 0.162T$
Electrical conductivity (S m^{-1})	$415\ln(T) - 2367$	$\frac{1}{(50.17 + 0.0838T - 1.7510^{-5}\ \ T^2)10^{-8}}$

$$h_i = -1.39210^{-5}\ \ T^2 + 0.02961T - 0.6227\left(W\ \ m^{-2}\ \ K^{-1}\right)$$

The scheme of the two simulation configurations is reported in Fig. 1. The real specimen temperature is expected to be between these two borderline cases.

2.4. Characterization

Thermo-gravimetric analysis (TGA) of the filament was carried out in Ar atmosphere with a heating rate of 20 °C min^{-1} (Netzsch STA 409 thermobalance). The Fourier transform infrared (FT-IR) spectra (Jasco FT/IR-4200) of as-printed, partially chemically debided and UHSed samples were acquired in attenuated total reflection (ATR) mode with a resolution of 4 cm^{-1}. Differential scanning calorimetry (DSC) tests were performed using a Mettler DSC30 calorimeter with a heating–cooling–heating cycle in the range 0 – 300 °C at ± 10 °C·min^{-1} flushing nitrogen at 100 mL·min^{-1}. The temperature and enthalpy of the endothermal and exothermal peaks were analysed by the Mettler Toledo Star software system.

Raman spectra were recorded with a microscope using a 532 nm laser (ThermoFisher DXR Raman). Phase composition was investigated by X-ray diffractometry (Bruker D8 Advance) in the 2θ-range 10–80° ($\Delta(2\theta) = 0.02°$ with a scan time of 1 s $step^{-1}$) using Cu Kα radiation

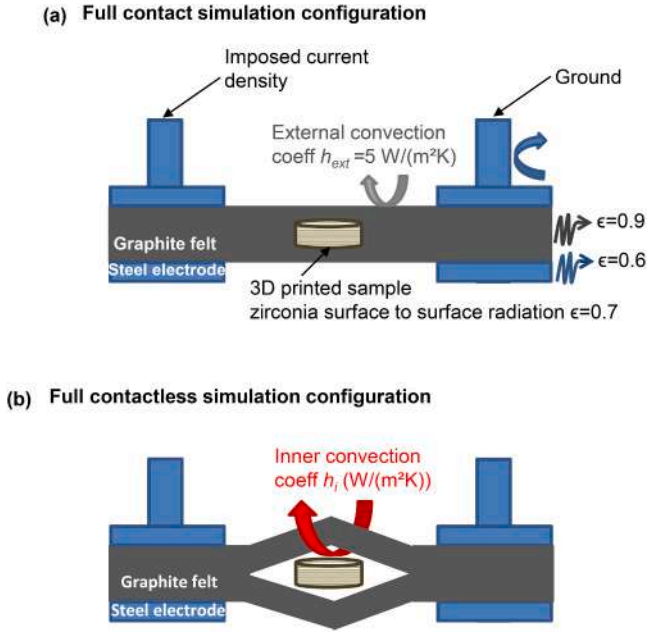

Fig. 1. Schematics of the two simulation configurations assuming (a) "full contact" of the felt with the sample and (b) "full contactless" configuration with the presence of inner convective thermal losses.

($\lambda = 1.5418$ Å). The X-ray source operated at 40 kV and 40 mA. The dilatometry of the chemically debinded samples was performed using a horizontal alumina dilatometer (Linseis L75) in an atmosphere of Ar (to simulate the UHS conditions) with a heating and cooling rate of 20 °C min^{-1}. The density of the sintered specimens was measured by Archimedes' principle using water as a buoyant medium, and the volume and size of the pores were assessed by mercury intrusion porosimetry (MIP) (Carlo Erba). The sintered samples were polished with diamond pastes and thermally etched for 1 h in Ar at 170 °C lower than the simulated UHS temperature to reveal the grain boundaries. The investigation of the microstructure of the polished samples was carried out using a scanning electron microscope (FIB-FE-SEM, Tescan SOLARIS) after sputter coating with a thin layer of graphite. The evolution of grain size in sintered samples was assessed from measurements of at least 100 grains with the help of ImageJ software [29]. The Vickers microhardness of the sintered samples was measured in 5 different regions on the polished cross-section using a Shimadzu micro hardness tester with a load of 300 gf for 15 s

3. Results

The weight loss recorded during the chemical debinding of the AMed components is reported in Fig. 2(a). A rapid decrease in weight was observed with increasing soaking time. The final weight loss after 4 h was about 8 wt%, but the system is substantially stable after only 1 h of soaking time in acetone, when a weight loss of 7.7 wt% was already recorded. Therefore, 1 h of chemical debinding was set as the optimized debinding time, and these samples were used for most of the UHS experiments. To validate the weight loss measurements, thermogravimetric analyses were performed on the samples chemically debinded for 1 h (Fig. 2(b)) both in air (to resemble conventional sintering) and in Ar (same atmosphere employed in the UHS experiments). The results show that the decomposition of the unsoluble binder component occurs between 280 °C and 520 °C, with a final weight loss of ≈ 6.6 wt% in both atmospheres, thus suggesting that when processing in Ar the amount of residual carbon is very limited. On the other hand, the weight loss of the as-received filament was ≈ 14 wt% (inset in Fig. 2(b)); hence we can infer that the chemical debinding allowed for the removal of just about half (≈53 wt%) of the starting binder in the AMed component. These results are perfectly consistent with the weight loss measured during chemical debinding.

FTIR spectra of the as-printed material evidence the presence of paraffin and vinyl-acetate which are declared components of the filament in the reference patent [37] (Fig. 2(c)). Furthermore, amidic groups have been detected. Chemical debinding induces the progressive reduction of peaks at 1710 and 1270 cm^{-1}, resulting after 60 min in a spectrum with the main peaks of amidic group –NH-CO- (at 3297 cm^{-1}: N-H stretching; at 1636 and 1543 cm^{-1}: >C═O stretching). The other peaks at 2915 and 2848 cm^{-1} are attributed to the C-H stretching. Therefore, we can infer that the main unsoluble binder fraction is made up of amidic compounds.

In addition, DSC analysis clearly shows the modification of the composition before and after debinding in acetone. Melting peaks are present at 50 °C (5.1 J g^{-1}) and at 85–130 °C (1.1 J g^{-1}) for the as-printed sample, while only a single large melting peak 110–150 °C (2.6 J g^{-1}) can be detected for the sample chemically debinded for 1 h (Fig. 2(d)). The cooling and the second heating scan (Fig. S4) evidenced exothermal and endothermal peaks, attributed to the crystallization and melting of the organic binder (in particular. the second heating scan confirmed the same melting temperature and enthalpy of the first scan for both samples). As a result, we can conclude that the chemical debinding method has completely removed the low-melting-point organic components.

Fig. 3 reports the cumulative pore volume for the different starting samples (as printed, chemically debinded for different soaking times in acetone and presintered at 950 °C) and confirms the removal of the

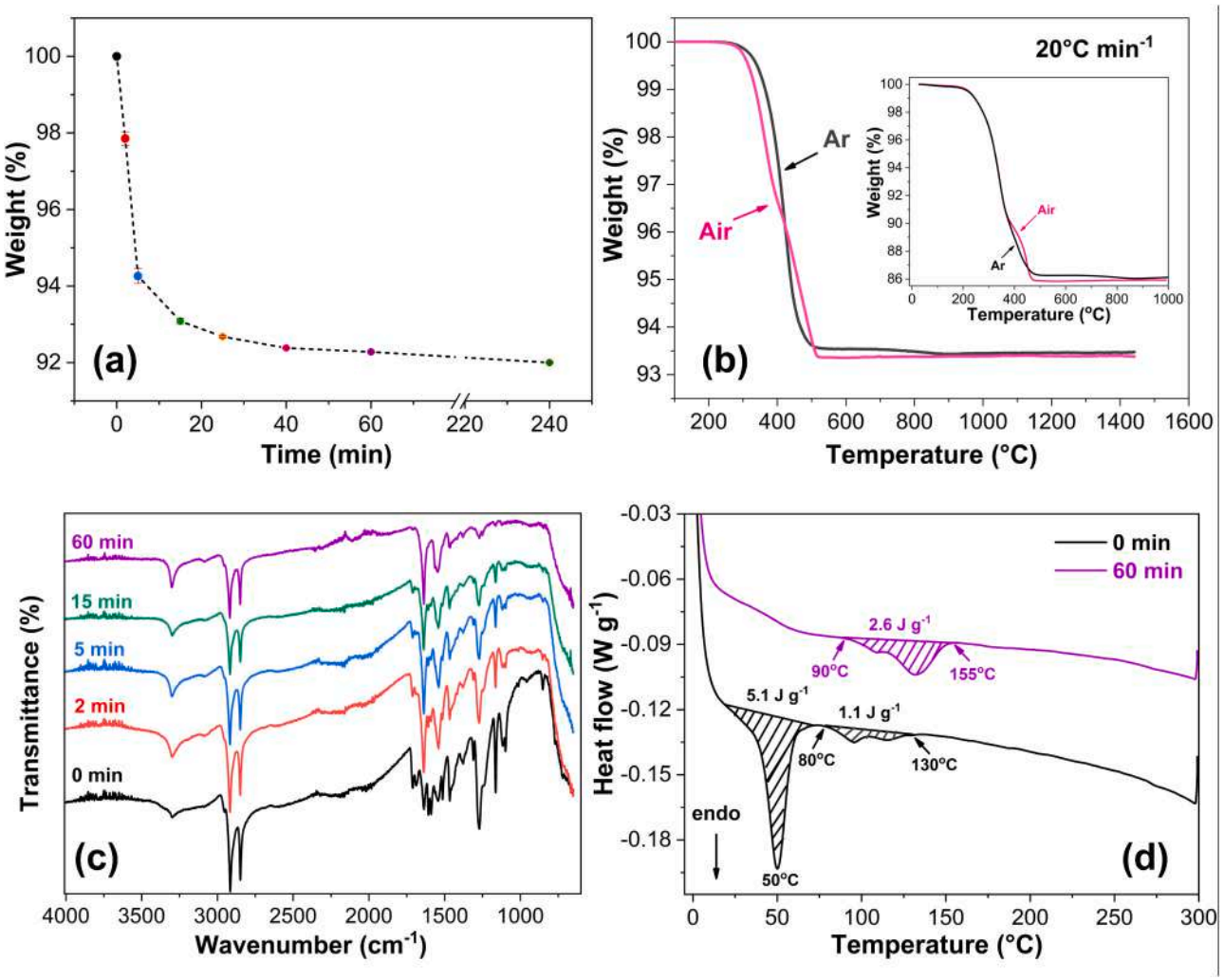

Fig. 2. (a) Weight loss of the as-printed sample as a function of the soaking time in acetone at 40 °C up to 4 h. (b) TGA analysis of the chemically debinded samples in acetone at 40 °C for 1 h in air and Ar (the inset shows the decomposition behavior of the as-received filament). (c) Fourier Transform Infrared Spectroscopy (FTIR) analysis of the as-printed samples at different soaking times (0, 2, 5, 15, 60 min) in acetone at 40 °C. (d) Differential Scanning calorimetry (DSC) curves (first heating scan) for the as-printed sample and the one after 60 mins in acetone.

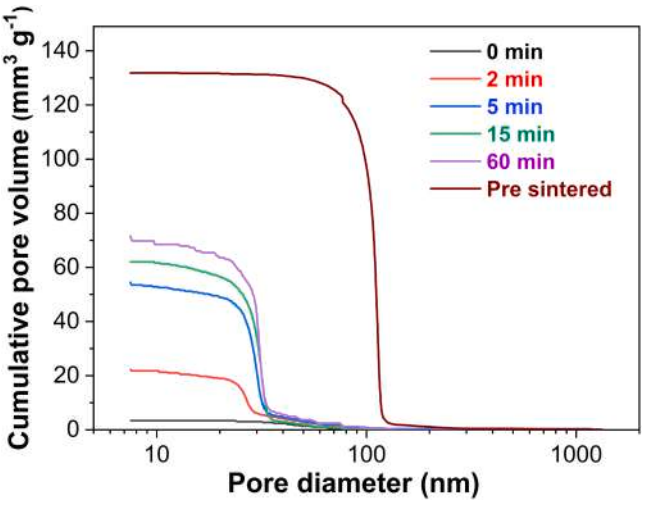

Fig. 3. Mercury intrusion porosimetry (MIP) results of the samples subjected to varying chemical debinding duration in acetone at 40 °C (0, 2, 5, 15, 60 min) and pre-sintering (950 °C for 1 h) treatment.

organic phase at different stages. The graph shows a significant increase in micro- and meso-porosity as a result of chemical debinding, which indeed increases with the soaking time in acetone. After presintering, macropores appear as the result of the polymer decomposition.

The dilatometric analysis of the chemically debinded samples (Fig. 4) reveals that densification starts at ≈ 1000 °C; a similar shrinkage behavior was recorded in the axial and radial direction, although a small deviation can be observed at high temperatures. Directional shrinkage is a typical outcome for AM components and arises from the layer buildup. Starting from 1300 °C to 1350 °C, the densification rate decreases and the shrinkage curve tends to flatten at 1500 °C, indicating almost complete densification. Accordingly, the samples after dilatometry were 96 % dense. The volumetric shrinkage is reported in the inset and is about 50 vol%, in agreement with the starting content of ceramic powder in the filament (≈50 vol%).

The effect of ultra-fast high-temperature sintering (26 A for 120 s) was evaluated on three different groups of samples: (i) as printed; (ii) partially chemically debinded for different times and (iii) pre-sintered (950 °C for 1 h). The as-printed (0 min, Fig. 5(a)), and pre-sintered (Fig. 5(b)) samples could not survive the ultra-fast heating. In the case of as-printed YSZ, the samples did not retain their shape, likely because of the relatively high amount of binder generating excessive decomposition gases upon heating. The samples pre-sintered at 950 °C retained

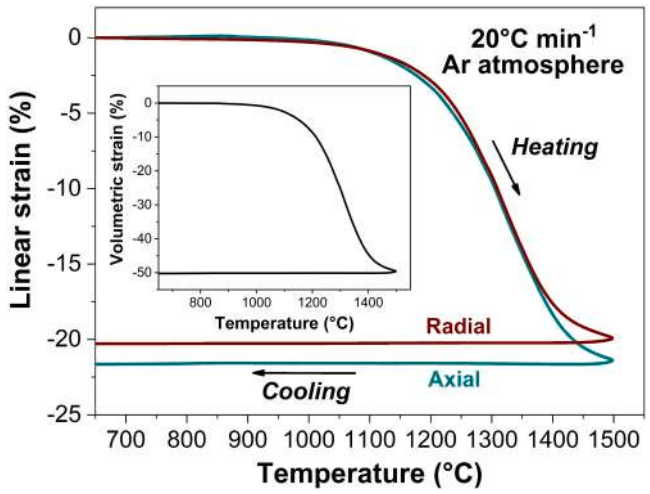

Fig. 4. Dilatometric radial and axial shrinkage curve of the chemically debinded sample in Ar. The inset reports the calculated volumetric shrinkage. Chemical debinding time = 1 h.

their shape; however, although they did not show any sign of damage after the pre-treatment, they were severely cracked after UHS. Conversely, the chemically debinded samples with soaking times greater than 15 mins were not damaged by the ultrafast heating, thus retaining their shape, not producing any cracks (even at the microscopic level) and showing promising sintering shrinkage (Fig. 5(a) and Fig. 6(a)). It is worth stressing that the sample chemically-debinded for 5 min already showed quite good results in terms of absence of defects and shape retentions, however, it was partially distorted after UHS. On these bases, 15 min is the minimum chemical debinding time recommended for the geometry of the present sample.

A summary of the different UHS experimental results, collected on different sample types and using different currents and dwelling times, is available in Table 2 and Fig. 6(a). The variation in relative density after UHS of the chemically debinded samples (1 h) is illustrated as a function of time and current in Figs. 6(b) and 6(c), respectively. There is substantially no densification with a holding time of 10 s or 15 s even at the maximum UHS current. Current (generating the Joule heat and the temperature needed for densification) and holding time are the most important factors that influence densification. By increasing either or both of them, the specimen density increases and almost full densification is observed for currents higher than 30 A with a dwell time of 60 s or more.

To investigate the origin of crack formation upon UHS of pre-sintered samples, some experiments were performed where pre-sintering was carried out in UHS under modest currents (18 A for 120 s; the results summary is in Table 2), to reach a temperature similar to the conventional pre-sintering one. Similar to pre-sintering in conventional furnaces, no damage was observed after pre-sintering in UHS and cooling down. However, when the UHS-pre-sintered sample was afterward subjected to a sintering step under 28 A, it was severely damaged. On the other hand, if no cooling was introduced between the 18 A and 28 A steps, the sample did not present any defects. To shed some light on the moment when cracks start to form, the UHS-pre-sintered sample (18 A, 120 s) was subjected to a second treatment at 18 A (120 s). In this case, no sintering occurred in the second UHS step (due to the low temperature reached), but some small cracks were produced. Finally, if the UHS-pre-sintered sample was subjected to a second treatment at 20 A, rather than 18 A, the sample cracked, even though it was still in the very early sintering stage (see the density results for UHSed samples under 20 A in Fig. 6(c)).

To model the temperature evolution by finite element modelling (FEM), the felt temperature was firstly calibrated without any sample. Fig. 7(a) and (b) show the variation of the power dissipated through the carbon felt as a function of time and current. The electric power and voltage (Fig. S5) under constant current decrease at the beginning of the process as a result of the electric heating of the felt (negative temperature coefficient for electric resistivity). The electrical parameters stabilize within ≈ 5 s, suggesting that the thermal equilibrium is virtually achieved. To calibrate the equilibrium felt temperature, the power needed to melt ≈ 10–20 mg of some high-purity metals (Fig. 7(c)) was measured. It is worth pointing out that the melting point of Ni was assumed to be 1326 °C, corresponding to the Ni-C eutectic, because SEM observations after melting always showed evidence of reactions between Ni and C. Therefore, it was possible to model the felt temperature as a function of the applied current (Fig. 7(d)), as an increasing function from about 1100 °C at 18 A to more than 1800 °C under 34 A.

The results in Fig. 7 were used to calibrate the electric conductivity of the felt and the convection fluxes on the surfaces used in FEM. These heating parameters were adjusted to fit the voltage curves and Cu, Ni, and Pt sample melting temperatures (the result is reported in Fig. S6).

Fig. 8 shows the models of the UHS set-up in full contactless and full contact configurations (a and b, respectively) developed for the FEM analysis. A probe positioned in proximity to the sample (as shown in the figure), indicates the location at which the simulated felt temperature was recorded.

After calibration and verification of the models, the heating of the approximated 3D printed zirconia specimen geometry was simulated assuming zirconia powder properties at 50 % relative density (i.e., a debinded yet not sintered sample). It should be noted that, while the endothermic effect associated to the binder decomposition would possibly cause a delay in the heating process, there are no legitimate grounds to expect any discrepancy in the simulated temperature during the steady state; furthermore, the sole potential error could anyway be an overestimation of the sample temperature by FEM. Thus, when comparing the FEM UHS temperature with that of conventional sintering, a conservative approach is ensured: in the event of an error, the actual sample temperature in UHS would be even lower than the one calculated by FEM.

FEM analysis points out that, albeit some thermal gradients exist in the UHS equipment, the equilibrium temperature distribution in the proximity of the sample is quite homogeneous in both full contactless and full contact UHS configuration (Figs. 9(a) and 10(a), respectively).

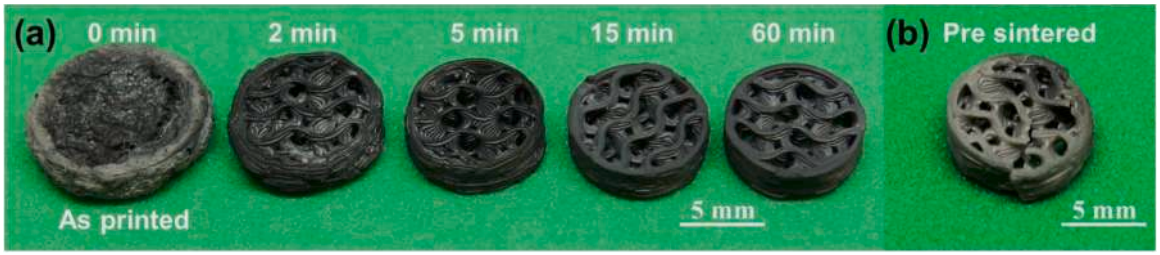

Fig. 5. Optical image of the UHSed (a) chemically debinded samples at different soaking times in acetone at 40 °C. (b) pre-sintered sample. UHS experiments was carried out at 26 A for 120 s.

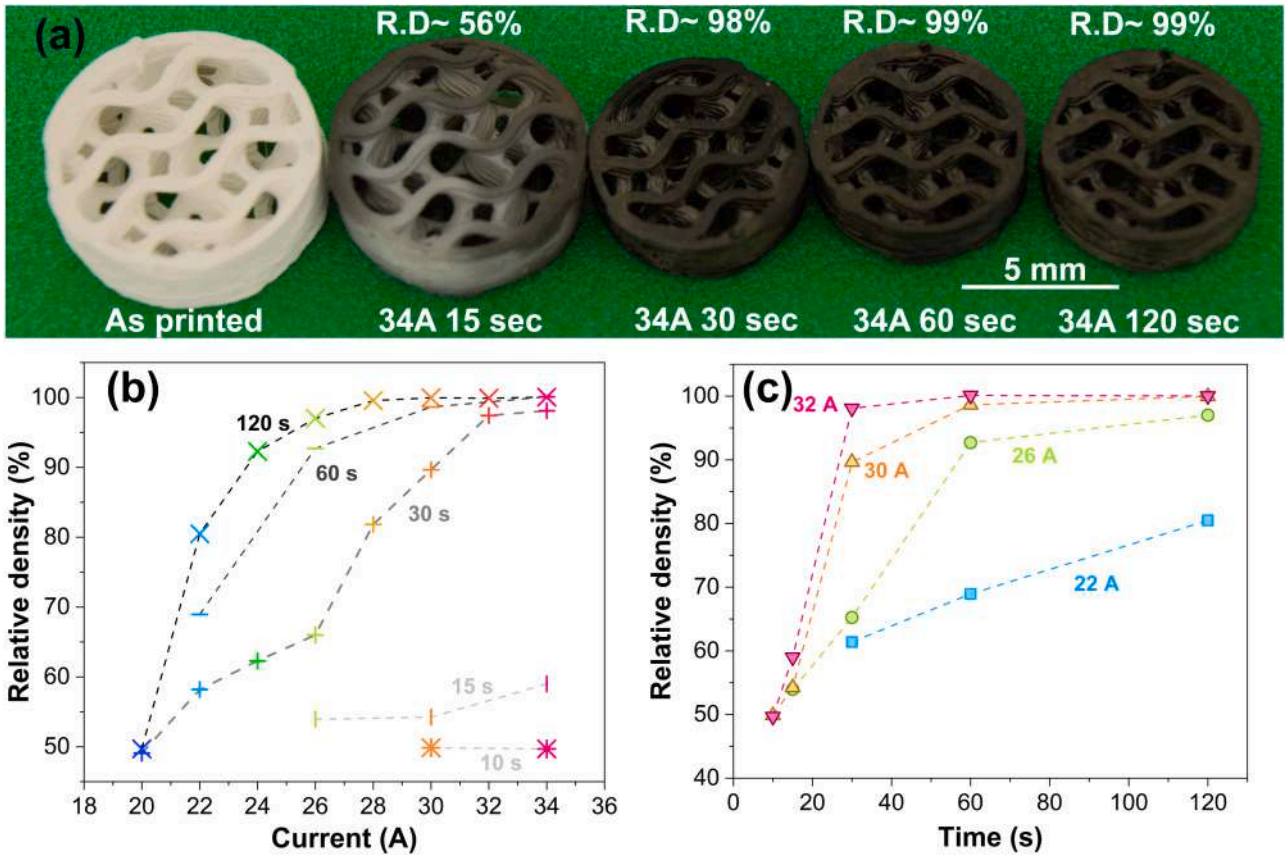

Fig. 6. (a) Optical images of the chemically debinded (1 h) UHS-ed sample at the maximum current of 34 A for different holding times (R.D = relative density of the samples). Relative density evolution of the chemically debinded and sintered samples as a function of (b) the pre-set current and (c) time.

Table 2
A summary of the different UHS conditions used in this research study with or without chemical debinding of 1 h in acetone at 40 °C.

Sample	UHS Conditions					Result
	1st sintering		Cooling	2nd sintering		
	Current (A)	Hold time (s)	Time (s)	Current (A)	Hold time (s)	
As printed	20–34	120	–	–	–	Shape not retained
Chemially debinded	20–34	10–120	–	–	–	Shape retained, no cracks, sintering dependent on the current and time
Chemically debinded and pre-sintered at 950 °C	26–34	120	–	–	–	Heavily cracked
Chemically debinded	18	120	–	28	120	Shape retained, no cracks, well sintered
Chemically debinded	18	120	60	28	120	Heavily cracked
Chemically debinded	18	120	60	18	120	Small cracks (detectable with OM),substantially not sintered
Chemically debinded	18	120	60	20	120	Small cracks (detectable with OM), early sintering stage

The simulated temperature evolution for the felt and the sample shows that, regardless of the current, the average sample temperature is always lower than that of the felt because of the radiative heat losses (as well as for the chimney effect in the full contactless configuration) (Figs. 9(c) and 10(c)).

In the contactless configuration, some temperature gradients can be identified within the sample (Fig. 9(b) for 30 A at 120 s); however, in the steady state of UHS (at the equilibrium) they appear quite modest, in a range of 80–110 °C depending on the current (Fig. 9(d)). Nevertheless, in the first ≈ 10–15 s of the process both the felt and the (pre-sintered) sample still have not reached a stable temperature and the (simulated) temperature difference in the sample peaks at ≈ 300 °C under the maximum tested current of 34 A.

In the full contact configuration, such gradients increase significantly: the simulated temperature difference reaches peaks of almost 800 °C in the first seconds of the process (at the maximum tested current of 34 A). It decreases thereafter, when equilibrium is reached, but it still stabilizes in a range of 390–460 °C depending on the current. The contactless configuration heating is slightly more stable because the sample is heated essentially by thermal radiation from the felt and both the felt inner surfaces and the samples surfaces are cooled by convection. These conditions make the heating less sensitive to the felt gradients and the felt thickness variation like for the full-contact configuration.

Fig. 11 compares the density evolution obtained from the dilatometric tests (Fig. 3) with that of the chemically debinded samples subjected to UHS for 120 s, as a function of the equilibrium average sample temperature (from FEM). One can observe that in both FEM configurations densification upon UHS is remarkably accelerated when compared with the conventional heating process in the dilatometer (20 °C min^{-1}). To make this statement more clear, let us take this example. The

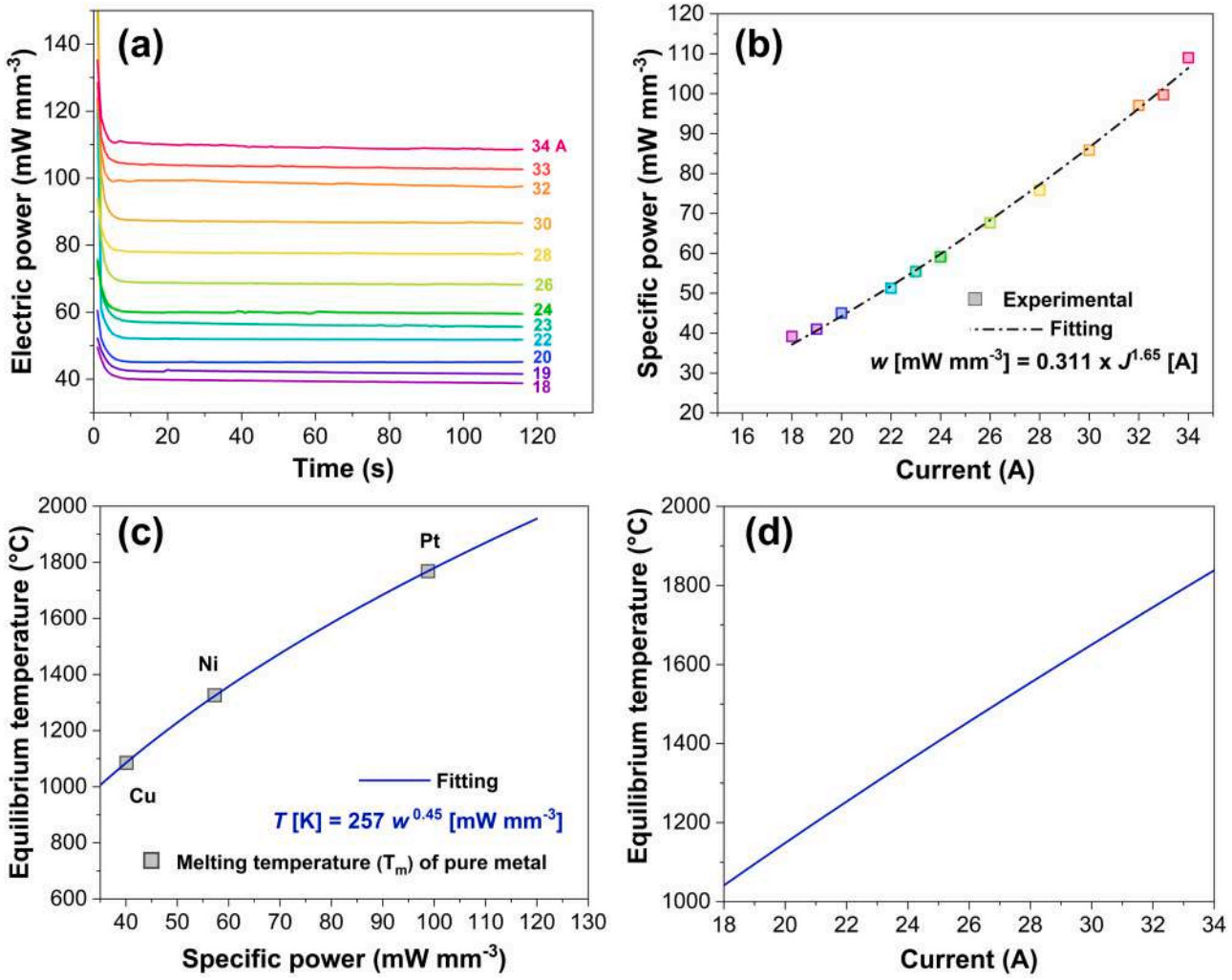

Fig. 7. (a) Variation of the electric power of the felt as a function of time. (b) Maximum electrical power dissipated in the carbon felt as a function of the pre-set current (measured experimental values and fitting curve). (c) Equilibrium felt temperature as a function of power dissipated in the felt; fitting was performed on the experimental values identified with the help of pure metals having defined T_m; for Ni, the Ni-C eutectic point at 1326 °C was selected as opposed to its melting temperature of 1455 °C. (d) Equilibrium felt temperature as a function of the applied electric current.

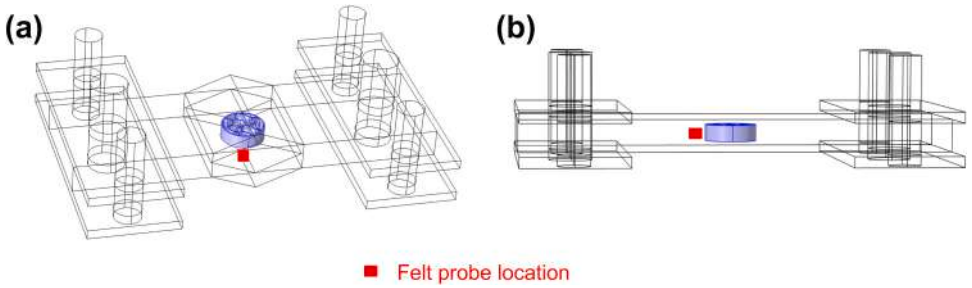

Fig. 8. UHS set-up with the probe location where the temperature was recorded for the (a) full contactless and (b) full contact configurations.

conventional dilatometry curve reveals that the samples are only 90 % dense at 1400 °C, on the other hand, at similar temperatures (30 A for both the UHS configurations), the sample reaches near-full density. This means that even though the samples experience similar sintering temperatures, the densification in UHS is faster as compared to the traditional sintering process.

To confirm the complete removal of organics from UHSed samples, FTIR spectroscopy was carried out on a sample subjected to 34 A for different holding times (Fig. 12(a)). The spectra of the chemical debinded sample reveal the presence of two main peaks at 2850 cm^{-1} and 2920 cm^{-1}, which are attributed to the symmetric and anti-symmetric stretching of C-H bonds, respectively [38], and the other peaks (not shown) are in agreement with those reported in Fig. 1(c). The peaks completely disappeared for treatments longer than 30 s. Micro-Raman analysis (Fig. 12(b)) revealed the presence of two distinctive features of the D-band and G-band at 1340 cm^{-1} at 1598 cm^{-1}, respectively, whose relative intensity and positions indicate the presence of turbostratic carbon originated from polymer

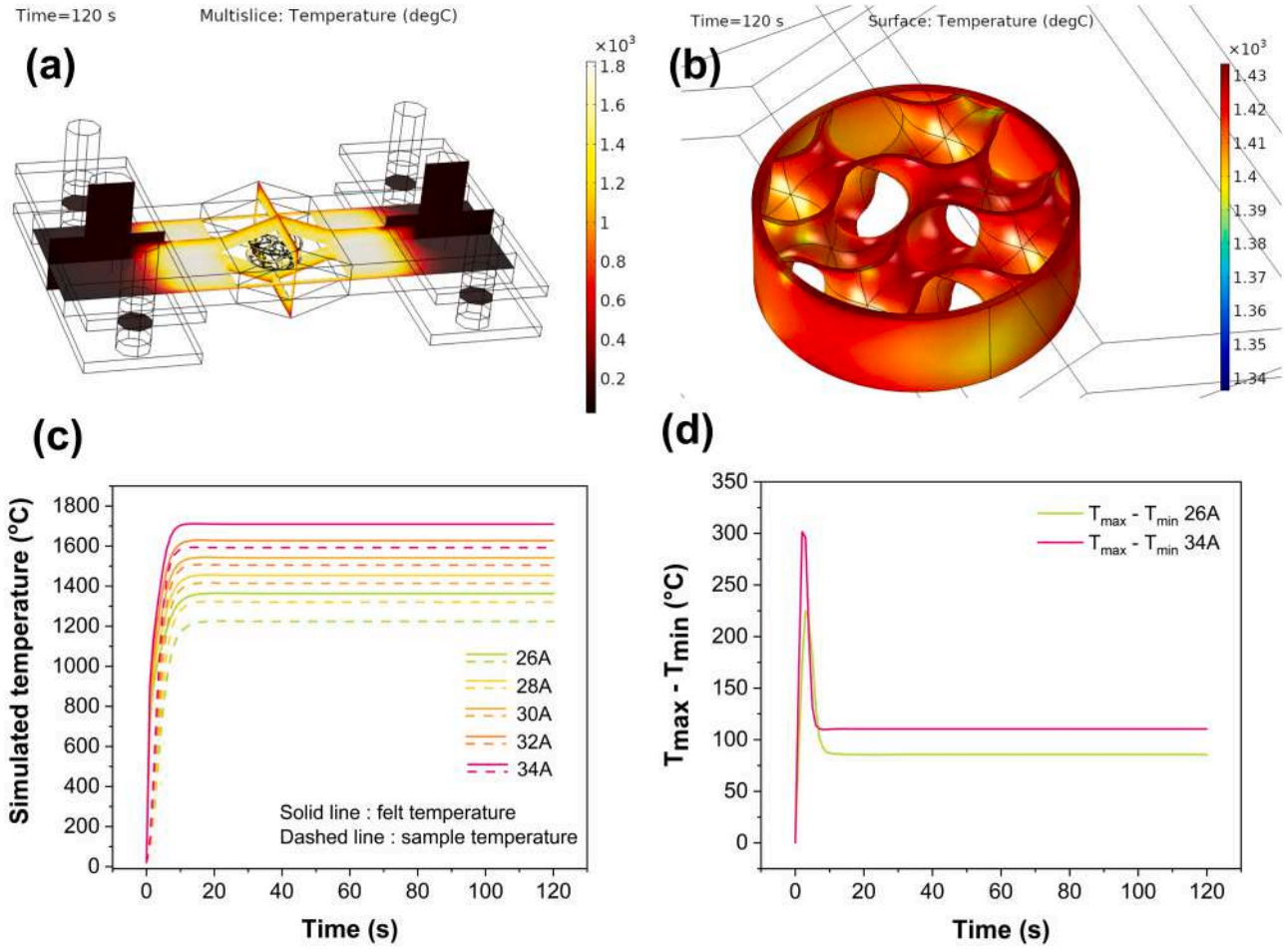

Fig. 9. Simulation results of the temperature distribution in the full contactless configuration: (a) UHS set-up (with focus on the carbon felt) and (b) debinded sample under 30 A current for 120 s (c) Results from FEM simulation of UHS at different maximum pre-set currents, showing the temperature evolution of the carbon felt (probe location at the inner surface) and the sintered sample (averaged throughout the 3D sample). (d) Simulated temperature gradient developed in the samples upon UHS with an applied current of 26 A and 34 A. The simulation does not include the endothermic effect associated with thermal debinding, it is therefore representative of pre-sintered samples. The heating process of chemically debinded samples is expected to be delayed.

decomposition [39,40]. As the UHS time increases, the relative intensity of the D and G peaks decreases, disappearing after 30 s. The spectra also reveal the presence of both monoclinic and tetragonal zirconia in the initial powder, whereas UHS samples treated for more than 10 s under 34 A contain only the tetragonal phase. These findings are consistent with the results of the X-ray diffraction analysis (Fig. 12(c)).

After UHS, the samples show a dark coloration (Figs. 5(a) and 6(a)). YSZ darkening is also observed in samples not showing any D/G features in Raman spectra, where it cannot be therefore attributed to the presence of carbon. To verify the presence of a possible reduction of YSZ under UHS, TGA analysis was carried out in air on a sample that was treated under 26 A for 120 s; the results are reported in Fig. 12(d) and show a limited but detectable mass increase (≈0.38 %) between 800 °C and 1200 °C. If the blackening was due to residual carbon from the binder, a weight loss at around 600 °C would have been expected upon heating in air, and such a feature was not observed.

The microstructures of highly dense samples as a function of holding time and current are shown in Fig. 12(e). The average grain size increases with current and holding time, as confirmed by previous findings [19]. The sample sintered at 30 A for 30 s shows a very fine microstructure with a mean grain size equal to 212 ± 71 nm; these grains are ≈ 20 % finer than those of the same material sintered conventionally (Fig. S7). Nevertheless, isolated pores can be detected at the triple junctions that disappeared at higher currents; samples sintered at 34 A for 30 s approach full density with limited grain growth (mean grain size ≈ 412 nm, similar to that of samples sintered conventionally in Ar). The microstructure appears homogeneous throughout the sample despite the temperature gradients predicted by the FEM analysis, as shown in Fig. 13. This suggests that the very short dwell time does not allow for the development of significant differences in grain growth. Further, by increasing the holding time to 120 s, grain growth becomes more evident, as the mean grain size reaches ≈ 644 nm.

The Vickers hardness of some UHSed and conventionally sintered samples is reported in Fig. 14. The hardness of the sample UHSed at 34 A for 30 s was comparable to that of the conventional samples (about 16 GPa). Furthermore, on decreasing the UHS current (30 A) or increasing the holding time (120 s), the hardness tends to decrease.

4. Discussion

The main outcome of the present work is that ultra-rapid debinding and sintering of 3D printed components are possible in a single step by UHS, when samples previously (partially) chemically debinded (residual organic content ≈6.6 wt%) are considered. Therefore, complex-shaped 3YSZ components with high density and no defects can be obtained in less than 2 min, including both thermal debinding and sintering. The UHSed materials completely consist of tetragonal zirconia (Fig. 12(c)), which makes them attractive for structural applications. The promising mechanical properties are confirmed by preliminary mechanical characterization by hardness test (Fig. 14) showing that optimized UHS

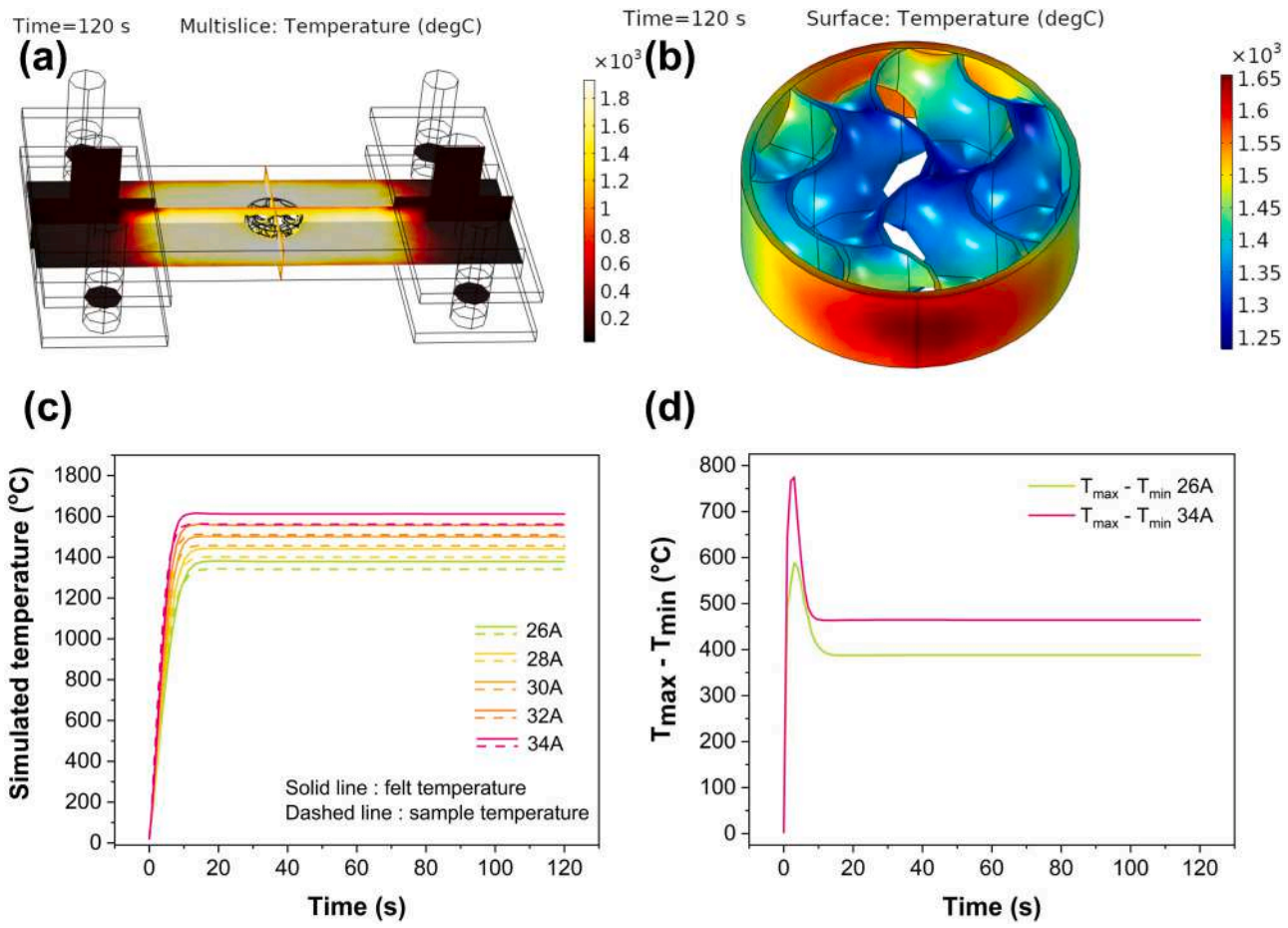

Fig. 10. Simulation results of the temperature distribution in the full contact configuration (a) UHS set-up (with focus on the carbon felt) and (b) debinded sample under 30 A current for 120 s (c) Results from FEM simulation of UHS at different maximum pre-set currents, showing the temperature evolution of the carbon felt (probe location at the inner surface) and the sintered sample (averaged throughout the 3D sample). (d) Simulated temperature gradient developed in the samples upon UHS with an applied current of 26 A and 34 A. The simulation does not include the endothermic effect associated with thermal debinding, it is therefore representative of pre-sintered samples. The heating process of chemically debinded samples is expected to be delayed.

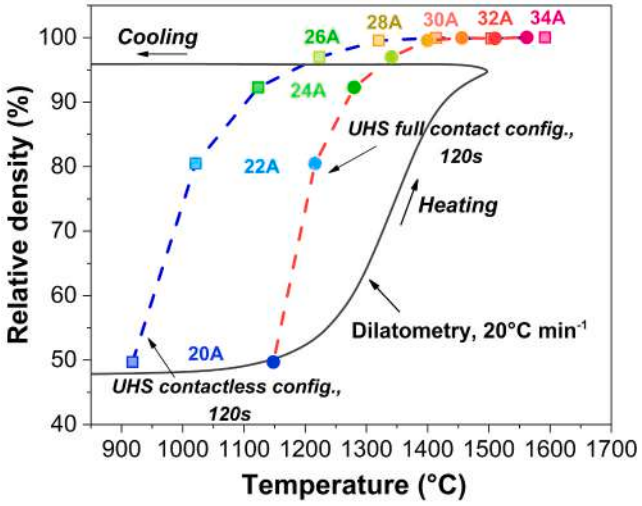

Fig. 11. Densification plot measured by dilatometry and simulated for contactless and full contact UHS configuration as a function of temperature. The UHS temperature corresponds to the highest value achieved by the average sample temperature (averaged over the sample volume) in a 120 s treatment under different currents (from FEM simulations). The data refers to samples chemically debinded for 1 h in acetone before UHS.

cycles lead to properties absolutely comparable to those of conventionally debinded and sintered materials.

The UHSed samples, different from those conventionally sintered in air, appear dark. This could be attributed to the presence of residual graphitic carbon traces only for samples subjected to short UHS treatments (≤15 s at 34 A according to Raman spectra); in fact, Raman spectra point out that graphitic carbon disappears for longer UHS treatments (Fig. 12(b)). This suggests that C reacts with YSZ, which becomes partially reduced under severe UHS conditions. The partial reduction is confirmed by the small but detectable weight gain recorded by TGA in air (Fig. 12(d)). The weight gain in the TGA measurement can therefore be attributed to the oxidation of partially reduced zirconia, and actually, the sample after TGA in air turns white. The absence of residual carbon is further confirmed by the absence of any weight loss in the 600–700 °C range, where graphitic carbon is expected to oxidize.

The chemical debinding step is crucial to obtain good results; the as-printed samples do not retain their shape if subjected directly to UHS. It should be noted that similar behavior can also be observed when as-printed (not chemically debinded) bodies are directly sintered in a conventional furnace. This can be attributed to the melting of the binder (range 50–110 °C) as well as to the substantial absence of interconnected pores in the as-printed materials (Fig. 3) which is pivotal for evacuating the gasses produced upon polymer pyrolysis. Although optimized chemical debinding requires up to 60 min of soaking in acetone at 40 °C, good results can already be obtained after 15 min (Fig. 5(a)). The formation of sufficient and continuous percolative

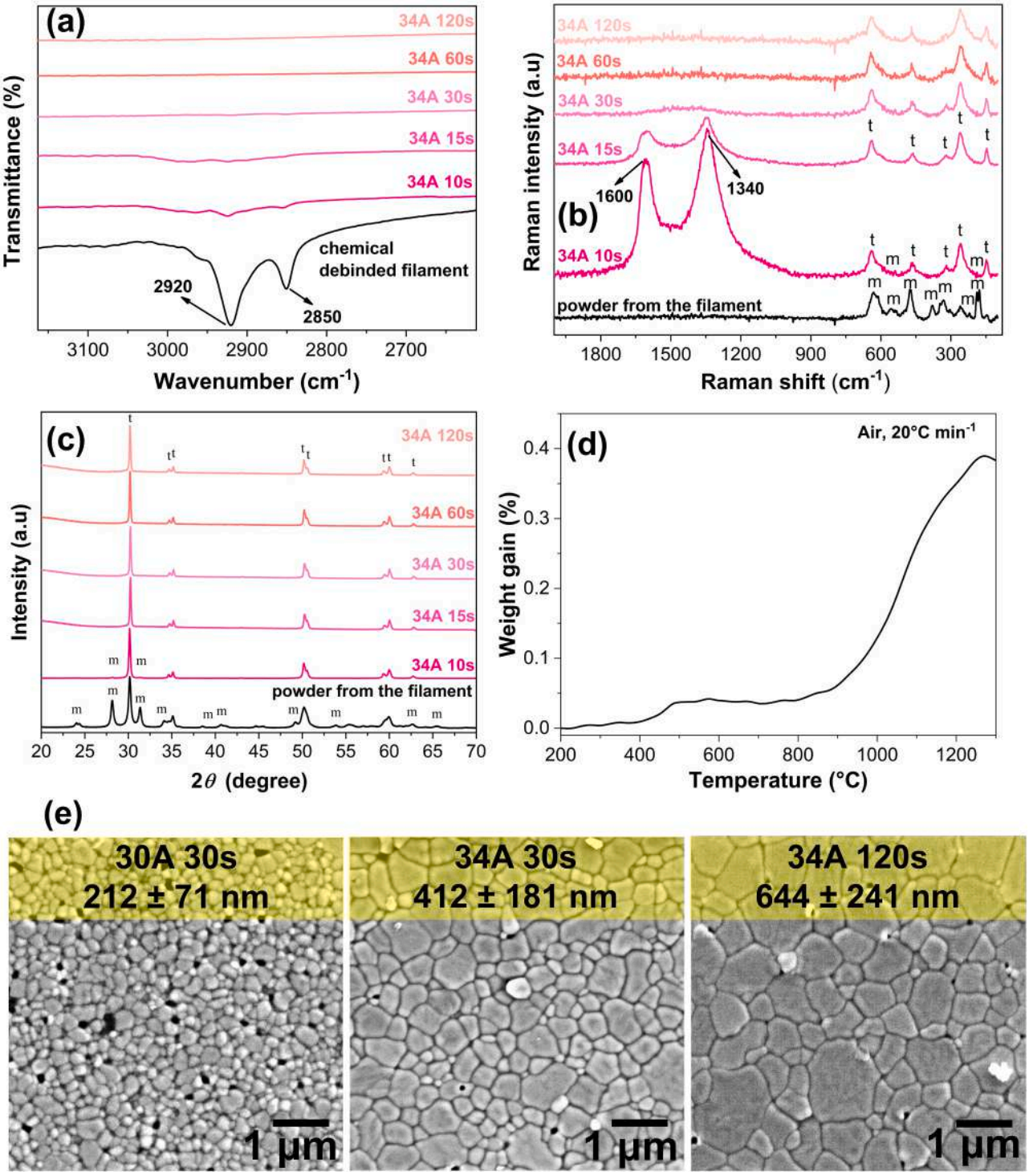

Fig. 12. (a) Fourier Transform Infrared Spectroscopy (FTIR), (b) Raman, (c) X-ray diffraction (XRD) spectra of chemically debinded sample (1 h in acetone) subjected to UHS under 34 A for different dwell times; the peaks of tetragonal and monoclinic zirconia are indexed as t and m, respectively. (d) TGA analysis of a UHS sample (26 A, 120 s) in air; (e) SEM micrographs showing the evolution of the microstructure with current and holding time.

channels of pores and the removal of the lower-molecular weight compounds during the chemical debinding certainly facilitate the evacuation of the gasses produced during the pyrolysis. As a result, the samples with a sufficient amount of interconnected open porosity (> 15 min of soaking time in acetone) could be rapidly sintered without any visible distortions or defects (Fig. 5(a)). It should also be noted that chemically debinding can be successfully applied only to 3D printed samples obtained by FFF and not to samples obtained by other AM technologies, such as Digital Light Processing, as in the latter case no soluble thermoplastic polymer is present after photo-crosslinking.

It is less straightforward to understand why several cracks are generated upon sintering in the pre-sintered samples, whereas no defects are present in the chemically debinded ones. One could argue that the formation of carbon residues from the polymer decomposition during UHS (confirmed by Raman spectra, Fig. 12(b)), facilitates heat diffusion and reduces thermal gradients while heating. However, this hypothesis

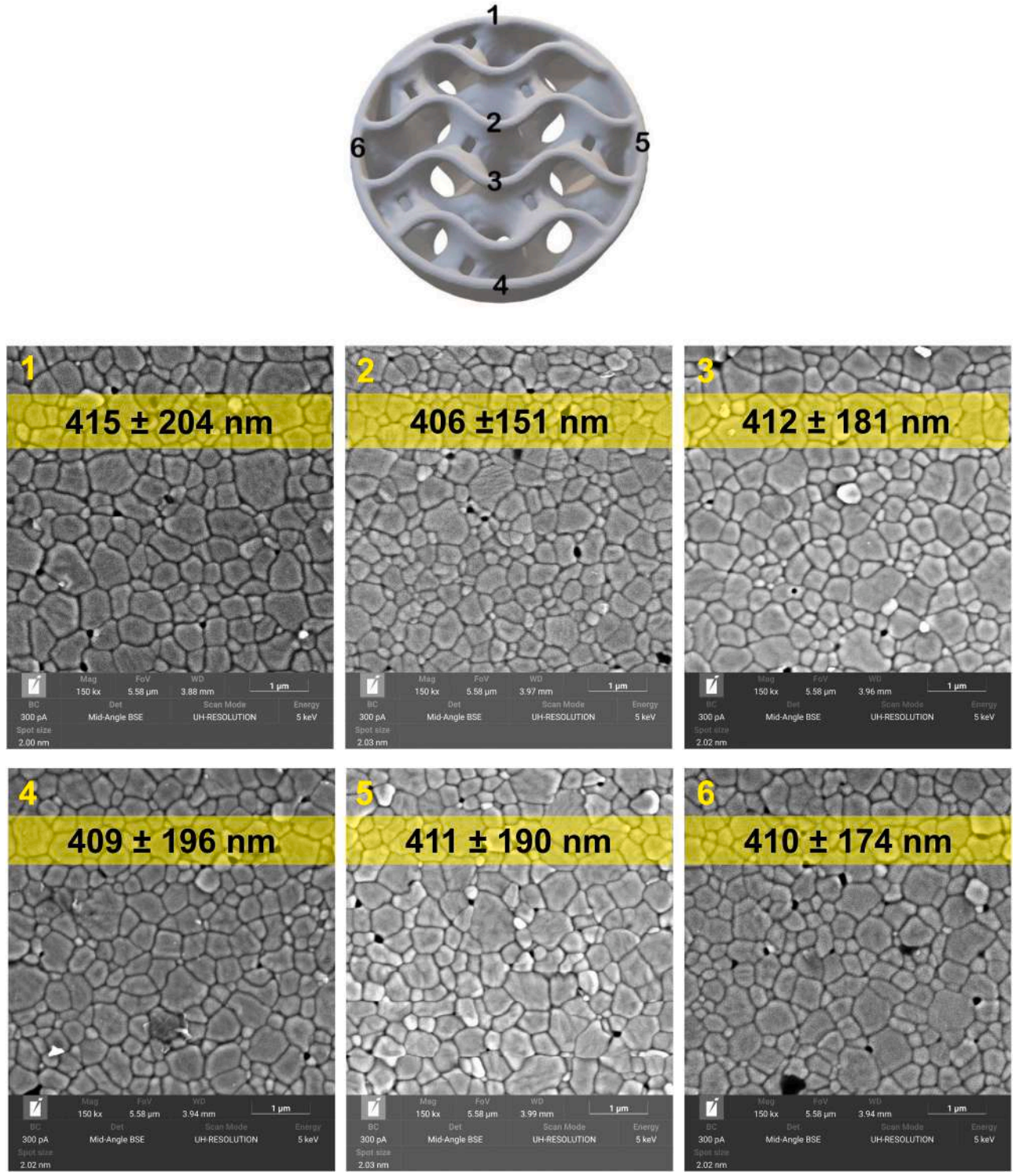

Fig. 13. Microstructural analysis (after UHS at 34 A for 30 s) of different regions on the sample surface. The microstructures refer to samples chemically debinded for 1 h in acetone before UHS.

is discredited by the fact that pre-sintering in UHS followed by a second UHS densification step (Table 2) leads to defects (although some carbon is indeed formed during UHS-pre-sintering).

The results summarized in Table 2 point out that the crucial step for crack formation in pre-sintered materials is associated with the absence of binder at the very initial sintering stages in UHS. As a matter of fact, both a "conventional" pre-sintered sample and samples pre-sintered in UHS at low current (18 A) already show some defects when UHSed in mild conditions (20 A), where only marginal densification occurs (Fig. 6 (b)). Moreover, FEM simulations demonstrate that large thermal gradients exist in the initial part of the UHS cycle (Figs. 9(d), 10(d)) where the sample is thought to enter the initial sintering stages. A possible explanation for the absence of cracks in chemically debinded materials includes therefore the following aspects:

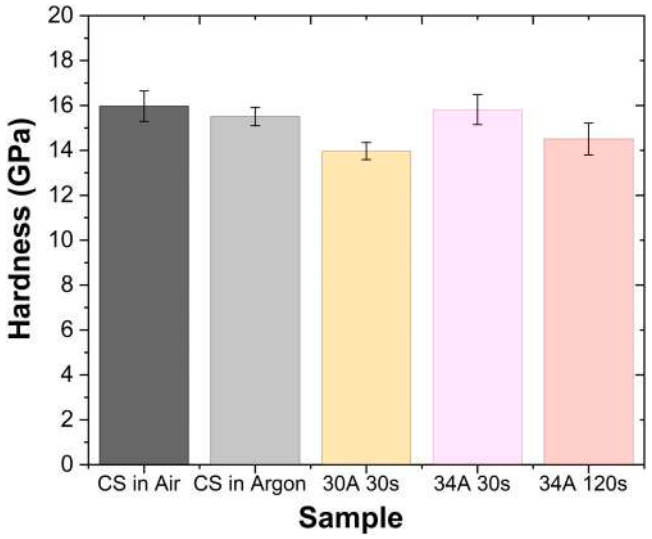

Fig. 14. Vickers hardness of chemically debinded (1 h in acetone) samples sintered in conventional and UHS conditions.

(i) The polymer decomposition (endothermic) moderates the heating schedule in the initial part of UHS when the largest thermal gradient is expected to develop according to Fig. 9(d) and Fig. 10 (d). This is confirmed by the fact that chemically-debinded samples under 34 A show only modest densification in the first 15 s. In the absence of the binder, the simulated temperature would approach ≈ 1600 °C, thus leading to substantial sintering (Figs. 9(c), 10(c)) which is not observed. Therefore, we can infer that the presence of some residual polymer after chemical debinding has some beneficial effects in terms of reducing the heating rates of the sample in the initial part of UHS, where most of the thermal gradients (and therefore stresses) develop.

(ii) Chemically-debinded materials might be more resistant to thermal shock compared with pre-sintered ones. In fact, it is reasonable to assume that their elastic modulus is lower due to the presence of pores and of an inter-particle polymer phase. Moreover, the polymeric matrix affords a higher mechanical strength than that displayed by a pre-sintered sample in which particle necking is still extremely limited. Interestingly, FT-IR analyses reveal the existence of some very limited residual organic binder (C-H bonds) after 15 s at 34 A (Fig. 12(a)) when the sample enters the initial sintering stages (proven to be critical for crack formation).

While the binder was removed, only negligible densification was observed at short holding times (10 or 15 s) regardless of the applied current (Fig. 6(b) and (c)). This implies that the thermal inertia of the setup does not allow the sample to heat up to a sufficiently high temperature necessary for sintering. Nevertheless, as soon as the target temperature is reached (i.e. for sufficient current and holding time), the samples were sintered to almost full density.

Finally, we can observe that UHS allows for an exceptional reduction of the actual sintering temperature (even more than 200 °C) while in parallel reducing also the sintering time when compared to conventional heating (Fig. 11). This conclusion relies on the sample temperatures obtained by FEM in either full contact or full contactless configuration, which can be considered the two limit conditions for the UHS treatment. FEM still provides the most credible measure of the local sample temperature, as the inner part of the felt is not accessible for measurement with a pyrometer in our experimental configuration (the felt is closed to reduce thermal gradients). On the other hand, thermocouples do not provide a credible measure of the felt temperature due to the presence of a metal shield (good thermal conductor) on the thermocouple tip causing a local drop in temperature. The mismatch between thermocouple temperature and actual sample temperature detected based on phase transitions has been already observed in a previous work [20].

Although the reduction of the sintering temperature in UHS might seem extraordinary, the result is credible as it matches the data obtained by other rapid sintering approaches such as flash sintering [41–43] and others [1]. The origin of such a huge effect of heating rates on sintering is still partially debated, but it already has strong theoretical and experimental bases: these include reduced grain coarsening, formation of out-of-equilibrium grain boundaries, reduced pore coordination, reduced pore-grain boundary separation under fast heating [42,43].

In general, the results prove that additively manufactured porous components are really suitable for rapid heating approaches, since the reduced size of the struts and the presence of macropores enable a fast and homogeneous heat exchange by radiation which produces dense microstructures with fine grains at relatively modest temperatures.

5. Conclusion

The feasibility of combining additive manufacturing and ultra-fast high-temperature sintering to print, debind, and sinter defect-free dense ceramic components with complex geometries was demonstrated in the present work. In fact, this approach of shaping and sintering complex-shaped ceramics has the potential to provide an energy-efficient alternative to conventional techniques such as pressureless sintering, hot pressing, etc., hence representing a small step in the direction of addressing the current energy crisis. Such a flexible, economically viable approach could be extended to a wide range of complex geometries and compositions.

Very remarkably, UHS allows for the combination of thermal debinding and sintering in a single step that takes only a few tens of seconds.While an appropriate chemical debinding step was shown to be indispensable to obtain a crack-free undistorted ceramic body upon UHS, its duration can also be reduced down to a few minutes. The sintered samples show a black coloration which can be ascribed either to the presence of graphitic carbon (short UHS times) or to a partial reduction of the oxide (especially in the most severe UHS conditions). The final density and microstructure evolution can be tailored by controlling the UHS current and time. Optimized UHS conditions lead to fully dense and homogeneous microstructures with sub-micrometric grains, absolutely comparable to those obtained by longer (≈5000 min) conventional debinding and sintering. UHS, therefore, enables a ground-breaking downshift of the heat treatment time (debinding/sintering) for fused filament fabricated ceramic components, which is reduced by even more than 99 %.

Declaration of Competing Interest

The authors declare that they have no known competing financial interests or personal relationships that could have appeared to influence the work reported in this paper.

Acknowledgment

Subhadip Bhandari gratefully acknowledges the CARIPARO Foundation, Padova, Italy, for his Ph.D. scholarship.

This study was carried out within the MICS (Made in Italy – Circular and Sustainable) Extended Partnership and received funding from the European Union Next-GenerationEU (PIANO NAZIONALE DI RIPRESA E RESILIENZA (PNRR) – MISSIONE 4 COMPONENTE 2, INVESTIMENTO 1.3 – D.D. 1551.11–10-2022, PE00000004). This manuscript reflects only the authors' views and opinions, neither the European Union nor the European Commission can be considered responsible for them.

This work is supported by the Italian Ministry of Economic Development (Ministero dello Sviluppo Economico, MISE) within the project "Processo Innovativo per la Ceramica Tecnica - PRINCE", F/310085/01/

X56.

Appendix A. Supporting information

Supplementary data associated with this article can be found in the online version at doi:10.1016/j.jeurceramsoc.2023.08.040.

References

[1] M. Biesuz, S. Grasso, V.M. Sglavo, What's new in ceramics sintering? A short report on the latest trends and future prospects, Curr. Opin. Solid State Mater. Sci. 24 (2020), 100868, https://doi.org/10.1016/j.cossms.2020.100868.

[2] W. Huisman, T. Graule, L.J. Gauckler, Centrifugal slip casting of zirconia (TZP), J. Eur. Ceram. Soc. 13 (1994) 33–39, https://doi.org/10.1016/0955-2219(94)90055-8.

[3] M. Jiménez-Melendo, C. Clauss, A. Domínguez-Rodríguez, G. de Portu, E. Roncari, P. Pinasco, High temperature plastic deformation of multilayered YTZP/ZTA composites obtained by tape casting, Acta Mater. 46 (1998) 3995–4004, https://doi.org/10.1016/S1359-6454(98)00066-4.

[4] R. Gadow, F. Kern, Pressureless sintering of injection molded zirconia toughened alumina nanocomposites, J. Ceram. Soc. Jpn. 114 (2006) 958–962, https://doi.org/10.2109/jcersj.114.958.

[5] A. Zocca, G. Franchin, P. Colombo, J. Günster, Additive manufacturing, Encycl. Mater.: Tech. Ceram. Glass 1–3 (2021) 203–221, https://doi.org/10.1016/B978-0-12-803581-8.12081-8.

[6] H. Kodama, Automatic method for fabricating a three-dimensional plastic model with photo-hardening polymer, Rev. Sci. Instrum. 52 (1981) 1770–1773, https://doi.org/10.1063/1.1136492.

[7] Y. Lakhdar, C. Tuck, J. Binner, A. Terry, R. Goodridge, Additive manufacturing of advanced ceramic materials, Prog. Mater. Sci. 116 (2021), 100736, https://doi.org/10.1016/j.pmatsci.2020.100736.

[8] Q. He, J. Jiang, X. Yang, L. Zhang, Z. Zhou, Y. Zhong, Z. Shen, Additive manufacturing of dense zirconia ceramics by fused deposition modeling via screw extrusion, J. Eur. Ceram. Soc. 41 (2021) 1033–1040, https://doi.org/10.1016/j.jeurceramsoc.2020.09.018.

[9] S. Cano, J. Gonzalez-Gutierrez, J. Sapkota, M. Spoerk, F. Arbeiter, S. Schuschnigg, C. Holzer, C. Kukla, Additive manufacturing of zirconia parts by fused filament fabrication and solvent debinding: selection of binder formulation, Addit. Manuf. 26 (2019) 117–128, https://doi.org/10.1016/j.addma.2019.01.001.

[10] V. Truxová, J. Šafka, J. Sobotka, J. Macháček, M. Ackermann, Alumina manufactured by fused filament fabrication: a comprehensive study of mechanical properties and porosity, Polym. (Basel) 14 (2022) 991, https://doi.org/10.3390/polym14050991.

[11] K. Sakthiabirami, J.-H. Kang, J.-G. Jang, V. Soundharrajan, H.-P. Lim, K.-D. Yun, C. Park, B.-N. Lee, Y.P. Yang, S.-W. Park, Hybrid porous zirconia scaffolds fabricated using additive manufacturing for bone tissue engineering applications, Mater. Sci. Eng.: C 123 (2021), 111950, https://doi.org/10.1016/j.msec.2021.111950.

[12] C. Wang, W. Ping, Q. Bai, H. Cui, R. Hensleigh, R. Wang, A.H. Brozena, Z. Xu, J. Dai, Y. Pei, C. Zheng, G. Pastel, J. Gao, X. Wang, H. Wang, J.-C. Zhao, B. Yang, X. (Rayne) Zheng, J. Luo, Y. Mo, B. Dunn, L. Hu, A general method to synthesize and sinter bulk ceramics in seconds, Science 368 (2020) (1979) 521–526, https://doi.org/10.1126/science.aaz7681.

[13] M. Kermani, D. Zhu, J. Li, J. Wu, Y. Lin, Z. Dai, C. Hu, S. Grasso, Ultra-fast high-temperature sintering (UHS) of translucent alumina, Open Ceram. 9 (2022), 100202, https://doi.org/10.1016/j.oceram.2021.100202.

[14] M. Kermani, J. Dong, M. Biesuz, Y. Linx, H. Deng, V.M. Sglavo, M.J. Reece, C. Hu, S. Grasso, Ultrafast high-temperature sintering (UHS) of fine grained α-Al2O3, J. Eur. Ceram. Soc. 41 (2021) 6626–6633, https://doi.org/10.1016/j.jeurceramsoc.2021.05.056.

[15] J. Dong, V. Pouchly, M. Biesuz, V. Tyrpekl, M. Vilémová, M. Kermani, M. Reece, C. Hu, S. Grasso, Thermally-insulated ultra-fast high temperature sintering (UHS) of zirconia: a master sintering curve analysis, Scr. Mater. 203 (2021), 114076, https://doi.org/10.1016/j.scriptamat.2021.114076.

[16] M.J.-H. Reavley, H. Guo, J. Yuan, A.Y.R. Ng, T.Y.K. Ho, H.T. Tan, Z. Du, C.L. Gan, Ultrafast high-temperature sintering of barium titanate ceramics with colossal dielectric constants, J. Eur. Ceram. Soc. 42 (2022) 4934–4943, https://doi.org/10.1016/j.jeurceramsoc.2022.04.056.

[17] R.-X. Luo, M. Kermani, Z.-L. Guo, J. Dong, C.-F. Hu, F. Zuo, S. Grasso, B.-B. Jiang, G.-L. Nie, Z.-Q. Yan, Q. Wang, Y.-L. Gan, F.-P. He, H.-T. Lin, Ultrafast high-temperature sintering of silicon nitride: a comparison with the state-of-the-art techniques, J. Eur. Ceram. Soc. 41 (2021) 6338–6345, https://doi.org/10.1016/j.jeurceramsoc.2021.06.021.

[18] T.P. Mishra, S. Wang, C. Lenser, D. Jennings, M. Kindelmann, W. Rheinheimer, C. Broeckmann, M. Bram, O. Guillon, Ultra-fast high-temperature sintering of strontium titanate, Acta Mater. 231 (2022), 117918, https://doi.org/10.1016/j.actamat.2022.117918.

[19] M. Ihrig, T.P. Mishra, W.S. Scheld, G. Häuschen, W. Rheinheimer, M. Bram, M. Finsterbusch, O. Guillon, Li7La3Zr2O12 solid electrolyte sintered by the ultrafast high-temperature method, J. Eur. Ceram. Soc. 41 (2021) 6075–6079, https://doi.org/10.1016/j.jeurceramsoc.2021.05.041.

[20] M. Biesuz, A. Galotta, A. Motta, M. Kermani, S. Grasso, J. Vontorová, V. Tyrpekl, M. Vilémová, V.M. Sglavo, Speedy bioceramics: rapid densification of tricalcium phosphate by ultrafast high-temperature sintering, Mater. Sci. Eng.: C. 127 (2021), 112246, https://doi.org/10.1016/j.msec.2021.112246.

[21] L. Spiridigliozzi, G. Dell'Agli, S. Esposito, P. Rivolo, S. Grasso, V.M. Sglavo, M. Biesuz, Ultra-fast high-temperature sintering (UHS) of Ce0.2Zr0.2Y0.2Gd0.2La0.2O2−δ fluorite-structured entropy-stabilized oxide (F-ESO), Scr. Mater. 214 (2022), 114655, https://doi.org/10.1016/j.scriptamat.2022.114655.

[22] S. Boldrini, A. Ferrario, S. Fasolin, A. Miozzo, S. Barison, Ultrafast high-temperature sintering and thermoelectric properties of n-doped Mg_2Si, Nanotechnology 34 (2023), 155601, https://doi.org/10.1088/1361-6528/acb15a.

[23] H.W. Li, Y.P. Zhao, G.Q. Chen, M.H. Li, Z.F. Wei, X.S. Fu, W.L. Zhou, SiC-based ceramics with remarkable electrical conductivity prepared by ultrafast high-temperature sintering, J. Eur. Ceram. Soc. 43 (2023) 2269–2274, https://doi.org/10.1016/j.jeurceramsoc.2022.12.025.

[24] J. Wu, Y. Lin, C. Hu, S. Grasso, D. Zhu, J. Li, A. Katz-Demyanitcz, A. Goldstein, Ultra-fast high-temperature sintering of transparent MgAl2O4, Ceram. Int 49 (2023) 19537–19540, https://doi.org/10.1016/j.ceramint.2023.03.018.

[25] S. Wang, T.P. Mishra, Y. Deng, L. Balice, A. Kaletsch, M. Bram, C. Broeckmann, Electric current-assisted sintering of 8YSZ: a comparative study of ultrafast high-temperature sintering and flash sintering, Adv. Eng. Mater. (2023) 2300145, https://doi.org/10.1002/adem.202300145.

[26] M. Kermani, C. Hu, S. Grasso, From pit fire to ultrafast high-temperature sintering (UHS): a review on ultrarapid consolidation, Ceram. Int 49 (2023) 4017–4029, https://doi.org/10.1016/j.ceramint.2022.11.091.

[27] R.-F. Guo, H.-R. Mao, Z.-T. Zhao, P. Shen, Ultrafast high-temperature sintering of bulk oxides, Scr. Mater. 193 (2021) 103–107, https://doi.org/10.1016/j.scriptamat.2020.10.045.

[28] F. Zuo, Q. Wang, Z.-Q. Yan, M. Kermani, S. Grasso, G.-L. Nie, B.-B. Jiang, F.-P. He, H.-T. Lin, L.-G. Wang, Upscaling ultrafast high-temperature sintering (UHS) to consolidate large-sized and complex-shaped ceramics, Scr. Mater. 221 (2022), 114973, https://doi.org/10.1016/j.scriptamat.2022.114973.

[29] A.-K. Hofer, A. Kocjan, R. Bermejo, High-strength lithography-based additive manufacturing of ceramic components with rapid sintering, Addit. Manuf. 59 (2022), 103141, https://doi.org/10.1016/j.addma.2022.103141.

[30] F. Sarraf, A. Hadian, S. v Churakov, F. Clemens, EVA-PVA binder system for polymer derived mullite made by material extrusion based additive manufacturing (in press), J. Eur. Ceram. Soc. (2022), https://doi.org/10.1016/j.jeurceramsoc.2022.10.009.

[31] Zetamix by Nanoe, White Zirconia Zetamix Filament, ⟨Https://Zetamix.Fr/En/Produit/White-Zirconia-Filament/⟩. (2023).

[32] C. Manière, T. Zahrah, E.A. Olevsky, Fluid dynamics thermo-mechanical simulation of sintering: Uniformity of temperature and density distributions, Appl. Therm. Eng. 123 (2017) 603–613, https://doi.org/10.1016/j.applthermaleng.2017.05.116.

[33] C. Manière, F. Borie, S. Marinel, Impact of convection and radiation on direct/hybrid heating stability of field assisted sintering, J. Manuf. Process 56 (2020) 147–157, https://doi.org/10.1016/j.jmapro.2020.04.075.

[34] G. Riquet, T. Grippi, C. Harnois, S. Marinel, C. Manière, Flash microwave sintering of zirconia by multiple susceptors cascade strategy, J. Eur. Ceram. Soc. (2023), https://doi.org/10.1016/J.JEURCERAMSOC.2023.04.004.

[35] C. Manière, G. Lee, E.A. Olevsky, Proportional integral derivative, modeling and ways of stabilization for the spark plasma sintering process, Results Phys. 7 (2017) 1494–1497, https://doi.org/10.1016/J.RINP.2017.04.020.

[36] SIGRATHERM® Download-Center | SGL Carbon, (n.d.). ⟨https://www.sglcarbon.com/en/markets-solutions/material-downloads/downloads-sigrathermr⟩ (accessed April 7, 2023).

[37] G. Bouchet-Doumenq, G. De La Lande De Calan, Compositions for 3D printing, WO202099484A1, 2020.

[38] Z. Li, W.-T. Jiang, Interlayer conformations of intercalated dodecyltrimethylammonium in rectorite as determined by FTIR, XRD, and TG analyses, Clays Clay Min. 57 (2009) 194–204, https://doi.org/10.1346/CCMN.2009.0570206.

[39] A.C. Ferrari, J. Robertson, Interpretation of Raman spectra of disordered and amorphous carbon, Phys. Rev. B 61 (2000) 14095–14107, https://doi.org/10.1103/PhysRevB.61.14095.

[40] M.A. Pimenta, G. Dresselhaus, M.S. Dresselhaus, L.G. Cançado, A. Jorio, R. Saito, Studying disorder in graphite-based systems by Raman spectroscopy, Phys. Chem. Chem. Phys. 9 (2007) 1276–1290, https://doi.org/10.1039/B613962K.

[41] W. Ji, B. Parker, S. Falco, J.Y. Zhang, Z.Y. Fu, R.I. Todd, Ultra-fast firing: effect of heating rate on sintering of 3YSZ, with and without an electric field, J. Eur. Ceram. Soc. 37 (2017) 2547–2551, https://doi.org/10.1016/j.jeurceramsoc.2017.01.033.

[42] Y. Zhang, J. Nie, J.M. Chan, J. Luo, Probing the densification mechanisms during flash sintering of ZnO, Acta Mater. 125 (2017) 465–475, https://doi.org/10.1016/J.ACTAMAT.2016.12.015.

[43] W. Ji, J. Zhang, W. Wang, Z. Fu, R. Todd, The microstructural origin of rapid densification in 3YSZ during ultra-fast firing with or without an electric field, J. Eur. Ceram. Soc. 40 (2020) 5829–5836, https://doi.org/10.1016/J.JEURCERAMSOC.2020.07.027.